Journal of Physics: Conference Series



# Characterization of turbulence under different stability conditions using lidar scanning data

# Characterization of turbulence under different stability conditions using lidar scanning data

**Raj K Rai[1], Larry K Berg[1], Rob Newsom[1], Colleen M Kaul[1], Jeffrey D Mirocha[2], Aditya Choukulkar[3], Alan Brewer[3], Yelena Pichugina[3], Robert Banta[3]**

[1]Pacific Northwest National Laboratory, Washington, USA, [2]Lawrence Livermore National Laboratory, California, USA, [3]National Oceanic and Atmospheric Administration, Colorado, USA

E-mail: raj.rai@pnnl.gov

**Abstract.** The spatiotemporal scales of turbulence in the boundary layer flow vary with the static stability of the atmosphere. For example, turbulence structures in unstable conditions are often found to be large and coherent, whereas the turbulent structures in stable conditions are relatively small and sporadic. To better understand the behavior of such turbulent structures under different atmospheric stability conditions in the lower atmosphere, herein, we use scanning lidar data collected over several months during the US Department of Energy's second Wind Forecast Improvement Project (WFIP 2) in 2016. The radial velocity data from scanning lidar were gathered along the conical surface (PPI mode) and were analyzed using proper orthogonal decomposition (POD) and spectral energy methods. The results from these analyses show that the turbulent structures in daytime unstable conditions are different from those present during nighttime stable conditions in terms of amount of energy and coherent structures. The POD energy is distributed more evenly in all the higher spatial modes in the daytime unstable case compared to the nighttime stable case. Besides characterizing the turbulence in the flow, the lidar data were also used to compare the simulated flow field generated from the WRF-LES framework (Weather Research and Forecasting - large-eddy simulation) with the scanning lidar data. The results from both simulated and lidar scanned data show similar structures – orienting the streak-like structure along the mean wind. This indicates that the streak-like structures can exist in the real atmosphere during unstable atmospheric condition cases.

## 1. Introduction

Turbulent structures present in the surface layer play a significant role to transfer momentum and energy within the boundary layer. The type and scale of turbulence structure often changes with the atmospheric stability which is a function of surface forcing. The spatial scale during the daytime unstable conditions could reach up to the depth of the boundary layer ($\sim z_i$), whereas it decreases to shallower depth during nighttime stable conditions due to the negative buoyancy [1]. Because of this wide range of spatio-temporal scales in the atmospheric boundary layer, it is challenging to decipher the behavior of turbulent structures using limited data (in space and time) from the traditional instruments. However, highly resolved, numerically simulated flow fields can provide details of the flow structures. In wind energy applications, large-eddy simulation (LES) is used to simulate the spatio-teporally resolved flow field of the atmospheric boundary layer [2, 3]. The simulated flow field is used either to study the wind resource or to

evaluate wind-farm performance [4, 5, 6, 7]. Although LES can provide resolved wind fields, its validation is difficult because of the lack of spatially resolved observation data.

Remote sensing devices, such as scanning lidar, can offer spatially resolved data near the surface layer. The scanning lidar is employed either to measure the wind components in the vertical direction (i.e., wind profile) or to scan across the prescribed plane using the combinations of elevation and azimuthal angles. The first method can provide all three wind components at a number of specified points with height (within the lidar's spatial resolution). In the wind energy community, several works [e.g., [2]] have employed the vertical profile of wind measured by scanning lidar. The second method provides radial velocity at a number of spatial locations by scanning the lidar along the prescribed plane with plan position indicator (PPI) and range height indicator (RHI) modes. This PPI or RHI mode only provides the radial velocity along the line of sight of the lidar. Scans can be done using a single lidar [8, 9] or multiple lidars aiming simultaneously at the same location at a time [10]. These lidar scanning studies [8, 10] mainly focus on the study of the characteristic of wind resource of a given location. Few researchers have utilized scanning lidar data to characterize turbulence and wakes of wind turbines (e.g., [11, 12]). However, no comprehensive study using ensemble data to characterize the turbulence under different stability conditions has been done.

This study uses radial velocity data obtained from a single scanning lidar in PPI mode at three elevation angles, ranging from 2.5°–6°. These data [13] were collected over a five-month period (May through September) near the Columbia Gorge, Oregon, during the US Department of Energy's Wind Forecast Improvement Project (WFIP-2) in 2016. Ensemble data under similar stability conditions are used to analyze the turbulence using proper orthogonal decomposition (POD) and spectral analysis. The results show that there are more coherent structures as well as more turbulent energy in unstable conditions compared to its counterpart stable conditions. In addition, simulated lidar data from an LES are also used to compare the flow structures with that from scanning data near the surface. For unstable stratification and moderate wind conditions, flow structures from both simulated and scanned flow fields show streak-like structures near the surface as in our past simulation work (e.g., [3]). In Section 2, the method used to analyze the scanning lidar data is discussed. The results and discussion are presented in Section 3, followed by the conclusion in Section 4.

## 2. Methods

The wind data were collected from scanning lidar deployed in the complex terrain with $\approx 100$ m change of elevation within the range of scanning of lidar. Figure 1 shows contours of terrain elevation and the location of the scanning lidar. Only the scanning area of 25° azimuth angle (i.e., in PPI mode) in the east is considered herein for cases with westerly flow. This east-sector contains 25 grid-points along the azimuthal direction and 100 spatial locations along the radial direction. To avoid bad data (i.e., below signal to noise ratio threshold $\approx$–30 dB) from distant points, only the 19 locations close to the location of lidar along the radial direction are used. The spatial resolution along the radial direction is 100 m, whereas the resolution along the azimuthal angle varies from 0.5° to 1° depending on the magnitude of the elevation angle. For example, the azimuthal resolution for the first two elevation angles (i.e., 2.5°, 4°) and third elevation angle (i.e., 6°) are 0.5° and 1°, respectively. However, we used 1° azimuthal angle resolution for all three elevation angles—2.5°, 4°, and 6°. Note that the time between two east-sector scans could vary from 3-min to several days.

The analysis of the turbulence structures using the radial velocity obtained from a scanning lidar is performed for 37 days of data for unstable conditions and 27 days stable conditions. These periods for analysis of unstable and stable cases were selected based on fair-weather days over the five-month period. Fair-weather conditions were assessed using the cloud fraction obtained from ceilometer [14]. The windows of time for unstable and stable conditions were

considered to be 1200–1559 PST(i.e., 4 hours) and 2200–0059 PST (i.e., 3 hours), respectively. For a given elevation angle, each hour of scanning lidar data produces four east-sectors (since the time between scans is 15 minutes). Therefore, the 37-day and 27-day scanning lidar data provide 1776 and 1296 east-sectors for unstable and stable conditions, respectively, considering all elevation angles. While using the east-sector data for analysis, we assume that each east-sector is a snapshot and all east-sectors have the same elevation angle. However, each east-sector contains radial velocities concatenated from 19 radial and 25 azimuthal locations. The time lag of radial velocity in each east-sector could have maximum of 25 s, and the east-sectors are from three elevation angles with maximum angle difference of 3.5°.

The east-sectors provide ensemble data for two stability conditions—unstable and stable. Within each stability condition, the amount of turbulence could vary due to different contributions of surface forcing and wind shear. To account for these factors, the entire set of east-sectors of each stability condition were further categorized into different groups based on average of radial velocity, $V_r$ (i.e., $< 5$, between 5 and 10, and $> 10$ m s$^{-1}$) and variance of radial velocity, $\rho^2$ (i.e., $<1.5$, between 1.5 and 3, and $>3$ m$^2$ s$^{-2}$) calculated from the radial velocity of all grid points (i.e., 19×25) of each east-sector. The three groups based on mean of radial velocity consist of 597, 598, and 619 east-sectors for unstable case, and 46, 524, and 421 east-sectors for stable case. Similarly, the three groups based on variance of radial velocity consist of 799, 561, and 333 east-sectors for the unstable case, and 182, 416, and 375 east-sectors for the stable case. The collection of east-sectors of each group contains dependent as well as independent east-sector data, depending on how far apart the data were taken. A collection of realizations could be assumed an ensemble when the east-sector are at least ≈30-min apart (i.e., approximate time for statistically independent to each other). The ensemble data of the east-sectors of each group were used to decompose into the basis function (i.e., POD modes) and time-varying coefficient (i.e., POD coefficients) using POD. Our previous work [3] used the POD tool for analyzing the coherent structure present in the flow. POD segregates the energy of the

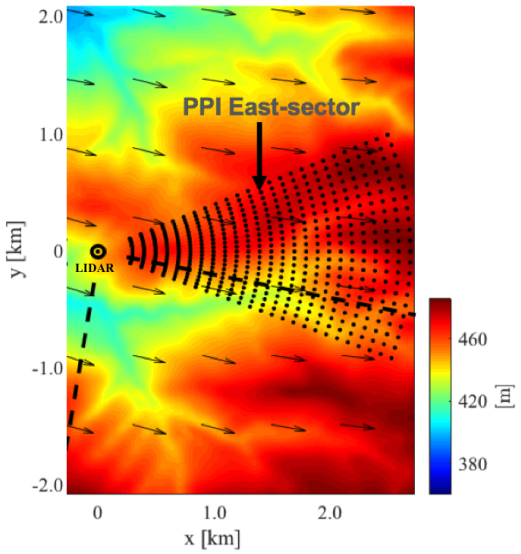


**Figure 1.**
Location of the scanning lidar and the grid points in the east-sector (i.e., obtained using PPI mode with constant elevation angle) overlaid on contours of terrain elevation. The vectors show mean wind direction during the daytime unstable condition. The dashed line shows the locations for RHI scanning mode (not used herein).

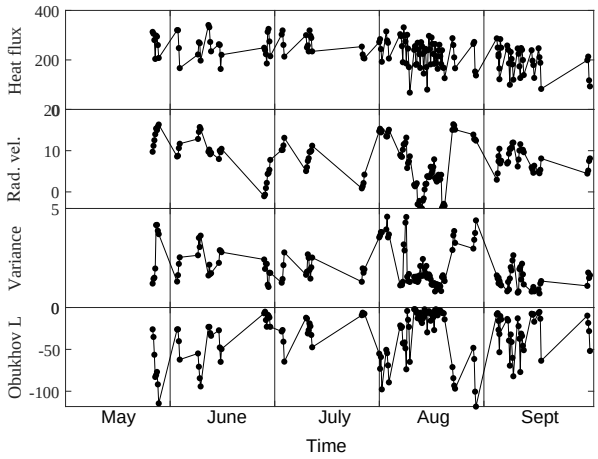


**Figure 2.**
Obukhov length (bottom row, in m), variance (third row, in $m^2\ s^{-2}$) and mean (second row, in $m\ s^{-1}$) of radial velocity, and heat flux (top row, in $W\ m^{-2}$) of each hour for the five-month period. Variance and mean of radial velocity are computed using east-sector data from scanning lidar, whereas heat flux and Obukhov length are measured data from meteorological station. The data showing here are only for the unstable condition case.

flow into the first few spatial modes depending on the amount of coherent structures present in the flow. Details of POD can be obtained in literature [15]. The basis functions derived from the east-sectors were used to evaluate the coherent structures present in the flow, whereas the POD energy was used to evaluate the energy present in different modes.

## 3. Results

The flow structures near the surface depend on the surface heat flux, which also determines the atmospheric stability. As mentioned in Section 2, we have selected 37 fair-weather days from the five-month period with positive heat flux for the analysis of unstable cases. The heat flux measurement is taken from a meteorological station [16], located near the scanning lidar, for the local time period 1200–1559 PST. Figure 2 (top row) shows time-series of heat flux in each hour. It should be noted that the number of measurements considered herein in each month are different, and the heat flux varies from 100 to 300 $W\ m^{-2}$ with a systematic decrease of its value from spring to fall. From these 37 days, the mean (Fig. 2, second row) and variance (Fig. 2 of radial velocity, third row) for each hour were calculated using radial velocity from four east-sector data. The mean radial velocity fluctuates from –2 to 15 $m\ s^{-1}$ (i.e., calm to windy). The variance of the radial velocity varies proportionately with the mean of radial velocity, which indicates the contribution of shear in generating turbulence. The Obukhov length (Fig. 2, bottom row) for all 37 days is negative, up to -100 m. The positive heat flux confirms that all the east-sectors considered herein represent the unstable condition. Similarly, negative heat flux was used to select the 27 days for the nighttime stable cases (not shown here). The variation in the heat flux and mean and variance of radial velocity near the surface could affect the flow structures. Therefore, we analyze the results of different groups of east-sector data categorized based on the mean and variances of radial velocity.

POD modes provide the basis function of the flow reconstruction, therefore they also characterize the turbulence structure in the flow. Figure 3 shows seven spatial POD modes (i.e., modes 1, 4, 7, 10, 13, 16, and 19) for five groups of east-sector data categorized based

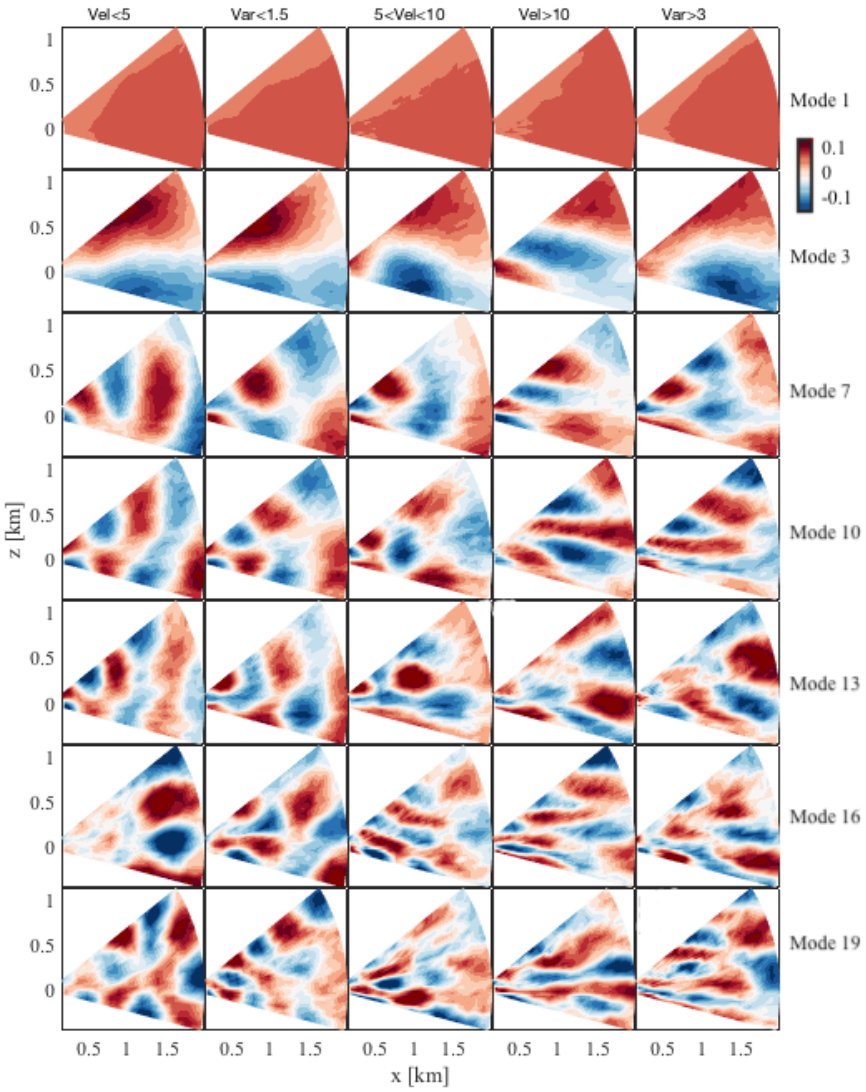


**Figure 3.**
Spatial POD mode of different groups of east-sector data based on mean of radial velocity <5 m $s^{-1}$ of 579 east-sectors (first column), variance of radial velocity <1.5 $m^2$ $s^{-2}$ of 799 east-sectors (second column), mean of radial velocity between 5 and 10 m $s^{-1}$ of 598 east-sectors (middle column), and mean of radial velocity >10 m $s^{-1}$ of 619 east-sectors (fourth column), and variance of radial velocity >1.5 $m^2$ $s^{-2}$ of 333 east-sectors (last column) for unstable condition case.

on mean and variance of radial velocity of each east-sector for the westerly flow and unstable daytime condition. The total number of spatial POD modes for each group is 475, resulting from 19 radial locations and 25 azimuthal locations. The seven modes in the first two columns are derived from east-sectors with low value of mean ($< 5$ m $s^{-1}$) and variance ($< 1.5$ $m^2$ $s^{-2}$) of radial velocity. The size and shape of structures in each mode shown look similar. The size of structures of POD mode decrease as the mode number increases, and the shape of the structure are open-cell without definitive orientation. As the group (i.e., column) moves from left to right, the mean and variance of each group of east-sector data increases. As a result, the shape of

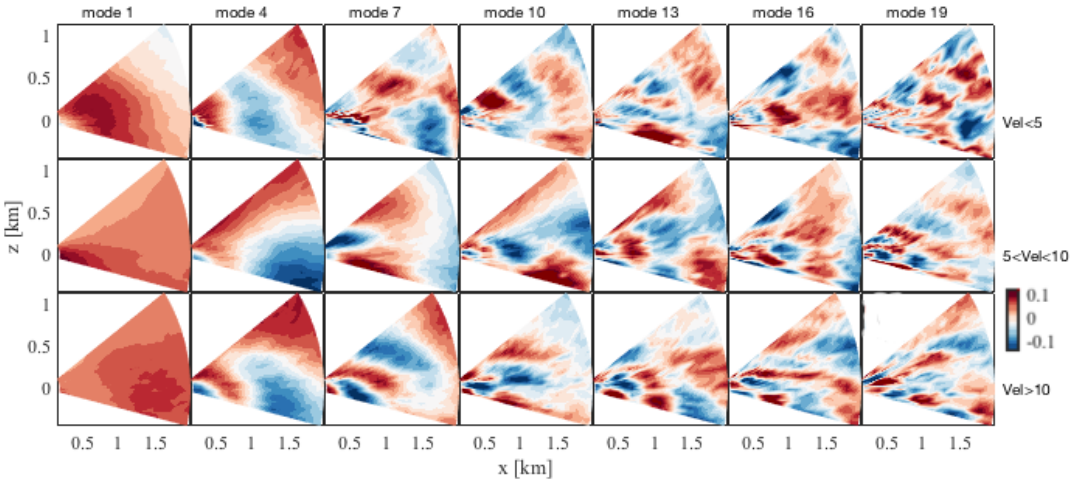


**Figure 4.**
Spatial POD mode of different groups of east-sector based on its mean of radial velocity <5 m $s^{-1}$ of 46 east-sectors (first row), mean of radial velocity between 5 and 10 m $s^{-1}$ of 524 east-sectors (middle row), and mean of radial velocity >10 m $s^{-1}$ of 421 east-sectors (bottom row) for stable condition case.

the structures of POD modes start becoming slender and orienting along mean wind direction, especially for the higher mode number, due to the increase of magnitude of radial velocity. For all groups of east-sector data, in general, the size of structures in spatial POD mode decreases with the increase of number of POD modes. The POD segregates most of its energetic coherent structures in the first couple of modes, therefore the size and shape of the POD modes in the first two rows shown in Fig. 3 appear to be similar. In addition to the unstable cases, POD analysis was also performed for the stable cases using 27 days of east-sector data. Figure 4 shows the seven POD modes (same mode numbers as shown for unstable conditions) for three groups of east-sector data categorized based on mean radial velocity. The shape and size of the structures of the first few modes for the case with mean radial velocity $< 5$ m $s^{-1}$ look different from the other two stable cases. The first POD mode of the case with mean of radial velocity <5 $ms^{-1}$ shows sharp gradient of mode values with little negative in the upper corner. Unlike the large and distinct structures in the unstable condition for case with mean radial velocity $< 5$ $ms^{-1}$, all modes in stable condition for the same velocity group show indistinct and completely different structures, that resemble the modes from cases with higher mean radial velocity for cases with unstable conditions. This shows the role of buoyancy in defining the shape of turbulent structures. The shape of structure of the POD modes, therefore, can predict the shape of turbulence structures in the flow as well as provide the basis to reconstruct the velocity field by operating the inner product between POD modes and time-dependent coefficient (POD coefficient).

Figure 5 shows the POD coefficients of the first 46 POD modes for the two stability conditions computed from six groups of east-sector data, categorized based on the mean and variance of radial velocity. The POD coefficients shown in the plot are the mean value of all the positive POD coefficients for the first 46 POD modes. Similar plots for the POD coefficients were obtained when using all the negative POD coefficients for the first 46 POD modes (not shown). Looking at Figure 5b for the stable condition, cases with radial velocity greater than 10 m

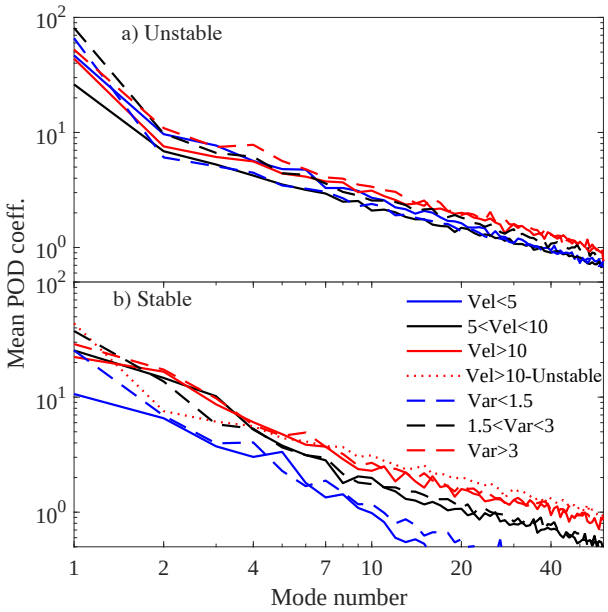


**Figure 5.**
Mean POD coefficient (only positive) of the first 46 modes for the different groups of east-sector based on its mean of radial velocity (<5 m $s^{-1}$, between 5 and 10 m $s^{-1}$, and >10 m $s^{-1}$) and variances of radial velocity (<1.5 $m^2$ $s^{-2}$, between 1.5 and 3 $m^2 s^{-2}$, and >3 $m^2$ $s^{-2}$ ) for a) unstable and b) stable stability conditions.

$s^{-1}$ and variances greater than 3 $m^2$ $s^{-2}$ produce higher values of POD coefficients for all 46 spatial POD modes. However, the POD coefficients for the case with mean radial velocity <5 m $s^{-1}$ shows the lowest magnitude for all modes. Recalling the POD modes for this mean radial velocity case (see Fig. 4, top row) and POD coefficients here, the reconstructed radial velocity would have the velocity fluctuations among the three groups of radial velocity cases. This implies that POD mode alone cannot predict the amount of turbulence in the flow. On the other hand, the POD coefficient derived for the unstable case (Fig. 3a) shows comparable magnitude for all six groups of east-sector mean and variance of radial velocity. This indicates that turbulent kinetic energy in all cases could be similar but their turbulent structures could be different, defined by the structures of their POD modes.

The amount of kinetic energy per unit mass (i.e., POD energy) for the first 200 spatial POD mode in two stability conditions is depicted in Fig. 6. It is noted that the curve of kinetic energy and that of POD coefficient are similar which tells that both quantities can represent the energy present in the flow. There is a large reduction of POD energy from the first to the second mode in unstable conditions, then the energy in the rest of the POD modes decrease smoothly in log-scale. On the other hand, the energy decrease smoothly for all POD modes in stable conditions. The large amount of energy present in the first mode signifies that there are significant coherent structures in the flow. The coherent structures are more evident in the daytime unstable conditions caused by both buoyancy and shear. In the first two modes of the unstable condition, the POD energy for the case with variance of radial velocity >3 $m^2$ $s^{-2}$ and the case with mean of radial velocity < 5 m $s^{-1}$ produced the highest POD energy, associated with large updraft structures. Compared to unstable conditions, the kinetic energy in the stable cases decreases smoothly in log-scale starting from the first mode without a sudden drop of

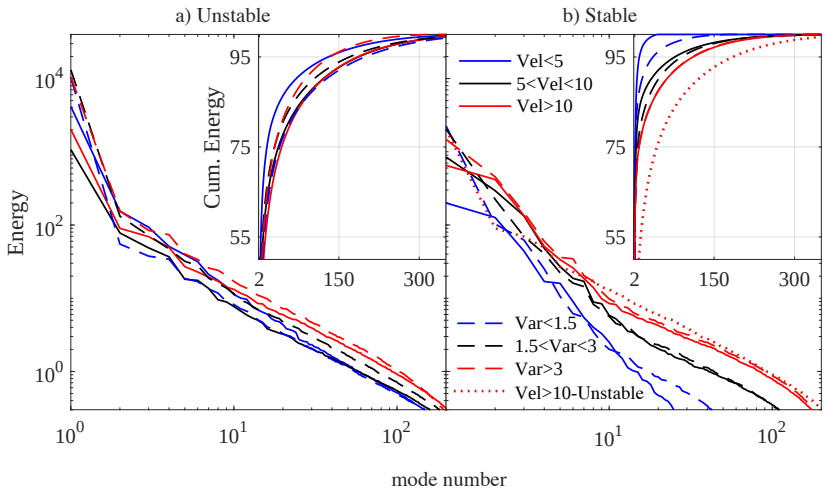


**Figure 6.**
POD energy in the first 200 modes and the cumulative energy for the 2–350 modes (shown in inset) for the different groups of east-sector data based on mean of radial velocity (<5 m $s^{-1}$, between 5 and 10 m $s^{-1}$, and >10 m $s^{-1}$) and variances of radial velocity (<1.5 $m^2$ $s^{-2}$, between 1.5 and 3 $m^2$ $s^{-2}$, and >3 $m^2$ $s^{-2}$ ) for a) unstable and b) stable stability conditions.

energy in second mode. The cases with high magnitude of mean and variance of radial velocity produced large amounts of kinetic energy, comparable to the unstable condition. The case with mean of radial velocity <5 m $s^{-1}$ produced the least kinetic energy. The large spread of energy for the same POD mode indicate that the kinetic energy in the stable condition is more sensitive to the magnitude of radial velocity. The inset in Fig. 6 shows the cumulative energy derived from the kinetic energy of second POD mode onward. The cumulative kinetic energy for unstable conditions shows that the kinetic energy is distributed into many POD modes, requiring almost (2–200) modes to capture 95% of energy of the flow. On the other hand, the cumulative kinetic energy for the stable condition only requires ≈(2–100) modes to represent 95% of energy of the flow. This indicates that turbulent energy is spread in more modes in unstable condition and their magnitude are also large compared to that of stable condition.

The spectral energy in wavenumber space provides information about the turbulence captured by the measurements. Figure 7 depicts the spectra of radial velocity computed from 19 radial and 25 azimuthal locations of east-sector data for the six groups categorized based on mean and variance of radial velocity. The mean spectral curve was obtained by averaging several spectral curves calculated from multiple instances of east-sector data. A single spectral curve was calculated using radial velocities from 19 radial locations. For unstable and radial position case (Fig. 7a, that use constant azimuth angle), the turbulence in the flow is highest for the cases with mean radial velocity (>10 m $s^{-1}$) and variance of radial velocity (> 3 $m^2$ $s^{-2}$). Most of cases follow the –5/3 slope (sub-inertial range) in the high wave number region [i.e., starting from the wavelength ≈ 1.2 km (the energy containing scale)]. The spectral plots, derived using 25 azimuthal locations at three radial distances from scanning lidar (i.e., 100 m, 500 m, and 1.9 km), are shown in Fig. 7c for the unstable condition. All the spectral energy curves approximately follow the –5/3 slope as their wavelengths are smaller than the energy-containing scale. On the other hand, the spectral energy calculated from radial velocity of 19 radial location for the stable condition (Fig. 7b) shows no turbulence for the case with mean of radial velocity <5 m $s^{-1}$ and variance of radial velocity < 1.5 $m^2$ $s^{-2}$. Other cases with larger mean and variance

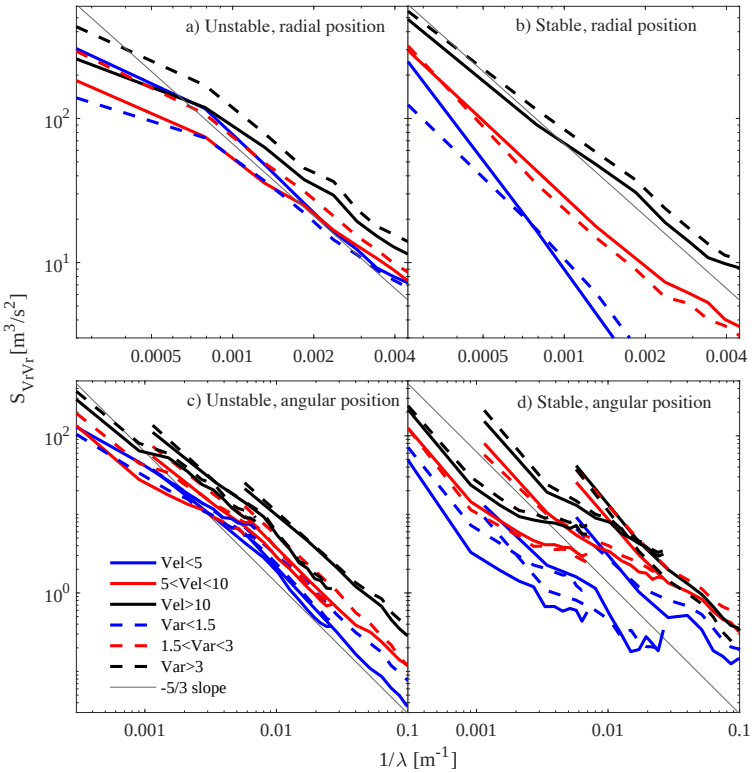


**Figure 7.**
Spectral energy for the different groups of east-sector based on its mean of radial velocity (<5 m s$^{-1}$, between 5 and 10 m s$^{-1}$, and >10 m s$^{-1}$) and variances of radial velocity (<1.5 m$^2$ s$^{-2}$, between 1.5 and 3 m$^2$ s$^{-2}$, and >3 m$^2$ s$^{-2}$ ) for a) unstable condition, radial position, b) stable condition, radial position, c) unstable condition, angular position, and d) stable condition, angular position. The term 'radial position' is used for the radial velocity data taken at 19 radial locations for a given azimuth angle, whereas the term 'angular position' is used for radial velocity data taken at 25 azimuthal locations at three distances 100 m, 500 m, and 1.9 km from the scanning lidar position.

of radial velocity captured the turbulence well over all wavenumbers, without showing a clear energy-containing scale as in unstable condition case. Similarly, the spectral curve calculated from the radial velocity of all 25 azimuthal locations at three radial position—100 m, 500 m, and 1.9 km— from the scanning lidar (Fig. 7d) showed an irregular curve at higher wavenumbers. This spike or increase of energy at high wavenumbers could be due to many reasons, such as 25 second time-lag or the presence of waves in the data, and needs more investigation.

In our previous work [3], the simulated wind field showed streak-like structures oriented along the mean wind near the surface for the moderate wind speed and unstable conditions. To compare with the scanning lidar data under a similar stability condition, a highly resolved flow field simulated with Weather Research and Forecasting (WRF)-LES was used to simulate the lidar data covering the east-sector. Figure 8 shows fluctuating radial velocity from the mean for lidar scanned data (PPI mode, top row) and simulated lidar data (bottom row) for the westerly wind at various times of the day. The contour for radial velocity in both flow depicts similar flow structures, indicating that the simulation can capture the realistic flow structure of the lower

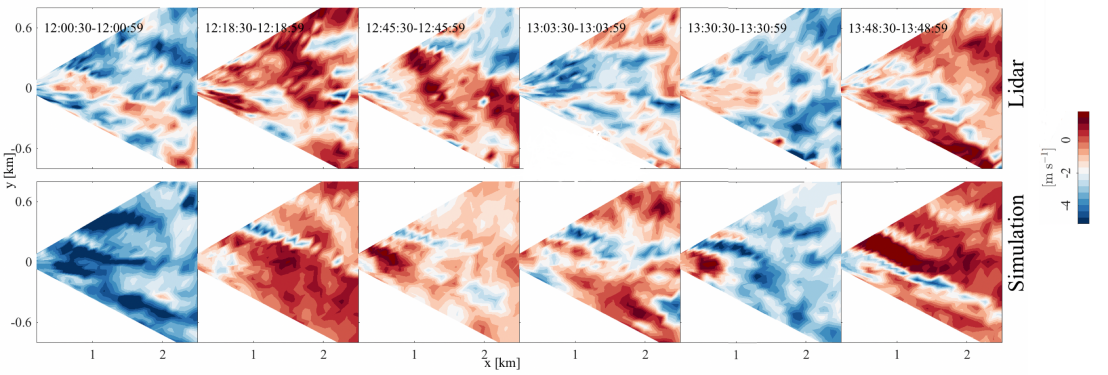


**Figure 8.**
Contour of radial velocity of east sectors at different times for scanning lidar (top row) and simulated flow (bottom row) in the unstable condition.

atmosphere.

## 4. Conclusions

Radial velocity data from scanning lidar collected during WFIP 2 field campaign were used to characterize the turbulence near the surface at two stability conditions—unstable and stable. Data from several fair-weather days were categorized into different groups based on magnitude and variance of radial velocity from east-sector data, which covers 25° azimuth angle PPI scan for a given elevation angle. The east-sectors from each group provide several realizations (i.e., an ensemble) as they contain statistically independent data. The ensemble were then used to analyze the POD modes and coefficients as well as spectral energy.

The results showed that the first POD mode contained more turbulent energy, and similarly, a large difference of turbulent energy exists between first and second mode in the unstable condition compared to that of the stable condition. The high content of energy in the first POD mode reveals that the unstable condition contains significant amount of coherent structures, possibly due to the organized updraft structures during the daytime. POD and spectral analysis showed that more energy is evenly spread in all higher modes in POD and large wave numbers in spectral analysis in unstable condition, suggesting more turbulence in the unstable condition compared to the stable condition case. The structure in the POD mode changed significantly with the magnitude of radial velocity and variance in the unstable conditions—from cellular-like structures to streak-like structures oriented along the mean wind for the increase of magnitude of radial velocity and variance. In contrast, the structure of POD modes in stable conditions is insensitive to varying magnitude of radial velocity and variances. However, the magnitude of POD coefficient increased with an increase of magnitude of radial velocity of the east-sector. Similarly, the spectral plot in the unstable cases showed energy cascade from energy containing scale to the sub-inertial range. However, there was no clear indication of energy-containing scales in stable condition case—all energy falls into the sub-inertial range. Overall, the result indicates that amount of turbulence could be different, although they have similar basis functions. Similarly, the positive buoyancy plays a great role in defining turbulence structures as well the amount of turbulence.

All data used herein have 100 m spatial resolution along the radial direction, which may not sufficiently capture fine-scale turbulence, especially at night. Multiple lidars with faster scanning rates may provide more highly spatially and temporally resolved data useful to turbulence study. In future work, we anticipate including more data from RHI mode, considering the neutral

condition case, and incorporating other sources of variability, such as cloudy days, southerly wind etc. into our analysis.

**Acknowledgments**
This research was supported by the Wind Energy Technologies Office of the US Department of Energy Office of Energy Efficiency and Renewable Energy. The Pacific Northwest National Laboratory is operated for the DOE by Battelle Memorial Institute under Contract DE-AC05-76RLO1830. The research was performed using computational resources sponsored by the Department of Energy's Office of Energy Efficiency and Renewable Energy and located at the Pacific Northwest National Laboratory. Lawrence Livermore National Laboratory's contribution prepared under Contract DE-AC52-07NA27344.

**References**
[1] Stull R B 2012 *An introduction to boundary layer meteorology* vol 13 (Springer Science & Business Media)
[2] Rai R K, Berg L K, Kosović B, Mirocha J D, Pekour M S and Shaw W J 2017 *Boundary-Layer Meteor.* **163** 69–89
[3] Rai R K, Berg L K, Kosović B, Haupt S E, Mirocha J D, Ennis B L and Draxl C 2019 *Monthly Weather Review* **147** 1007–1027
[4] Porté-Agel F, Wu Y T, Lu H and Conzemius R J 2011 *Journal of Wind Engineering and Industrial Aerodynamics* **99** 154–168
[5] Churchfield M J, Lee S, Michalakes J and Moriarty P J 2012 *Journal of turbulence* N14
[6] Mirocha J, Kosovic B, Aitken M and Lundquist J 2014 *Journal of Renewable and Sustainable Energy* **6** 013104
[7] Rai R K, Gopalan H, Sitaraman J, Mirocha J D and Miller W O 2017 *Environmental modelling & software* **94** 172–185
[8] Newsom R, Calhoun R, Ligon D and Allwine J 2008 *Boundary-layer meteorology* **127** 111–130
[9] Newsom R K, Berg L K, Shaw W J and Fischer M L 2015 *Wind Energy* **18** 219–235
[10] Newman J F, Bonin T A, Klein P M, Wharton S and Newsom R K 2016 *Wind Energy* **19** 2239–2254
[11] Aitken M L and Lundquist J K 2014 *Journal of Atmospheric and Oceanic Technology* **31** 1529–1539
[12] Peña A, Mann J and Dimitrov N K 2017 *Wind Energy Science* **2** 133–152
[13] Atmosphere to Electrons (A2e). 2017. wfip2/lidar.z04.b0. Maintained by A2e Data Archive and Portal for U.S. Department of Energy, Office of Energy Efficiency and Renewable Energy. DOI: 10.21947/1418023. Assessed: 01 July 2019
[14] Atmosphere to Electrons (A2e). 2017. wfip2/ceil.z01.00. Maintained by A2e Data Archive and Portal for U.S. Department of Energy, Office of Energy Efficiency and Renewable Energy. DOI: 10.21947/1349236. Assessed: 10 July 2019
[15] Holmes P, Lumley J L, Berkooz G and Rowley C W 2012 *Turbulence, coherent structures, dynamical systems and symmetry* (Cambridge university press)
[16] Atmosphere to Electrons (A2e). 2017. wfip2/met.z15.b0. Maintained by A2e Data Archive and Portal for U.S. Department of Energy, Office of Energy Efficiency and Renewable Energy. DOI: 10.21947/1401989. Assessed: 10 July 2019